Shallow water analysis of gravity current flows past isolated obstacles

By E. GONZALEZ-JUEZ AND E. MEIBURG

Department of Mechanical Engineering, University of California at Santa Barbara

(Received ?? and in revised form ??)

The flow of a partial-depth lock-exchange gravity current past an isolated surface-mounted obstacle is studied by means of two-dimensional direct numerical simulations and steady shallow water theory. The simulations indicate that the flux of the current downstream of the obstacle is approximately constant in space and time. This information is employed to extend the shallow-water models of Rottman *et al.* (1985) and Lane-Serff *et al.* (1995), in order to predict the height and front speed of the downstream current as functions of the upstream Froude number and the ratio of obstacle to current height. The model predictions are found to agree closely with the simulation results. In addition, the shallow water model provides an estimate for the maximum drag that lies within 10% of the simulation results, for obstacles much larger than the boundary layer thickness.

1. Introduction

Gravity currents form in natural environments and engineering applications when a heavier fluid propagates into a lighter one in a predominantly horizontal direction (Simpson (1997)). The study of gravity current flows around surface-mounted obstacles has been motivated by practical applications such as the design of barriers for the containment of heavy hazardous gases (Rottman *et al.* (1985); Lane-Serff *et al.* (1995)), powder snow avalanches (Hopfinger (1983)), and dilute ash flows (Woods *et al.* (1998)); the development of strategies for controlling sedimentation (Oehy & Schleiss (2007); Kneller *et al.* (1999)); and the need to obtain estimates of the dynamic loads on submarine structures from the impact of gravity and/or turbidity currents (Ermanyuk & Gavrilov (2005*a*,*b*); Gonzalez-Juez *et al.* (2007, 2008*a*,*b*)).

When a gravity current encounters an isolated, impermeable surface-mounted obstacle, its head first is deflected upwards and later reattaches to the bottom wall. The current eventually reestablishes itself downstream of the obstruction, and the flow around the obstacle becomes quasisteady (Ermanyuk & Gavrilov (2005*a*,*b*); Gonzalez-Juez *et al.* (2008*a*)). Such quasisteady flow long after the impact stage can be modeled based on the existing steady shallow water theory for the flow of a denser fluid under a lighter fluid past bottom topography (e.g. the monographs by Turner (1973) and Baines (1995) among others). This well-studied problem is characterized by the ratio of the obstacle height to the undisturbed dense fluid layer height D/d_l, the ratio of the heights of the undisturbed dense fluid layer and the light fluid layer d_l/d_u, and the Froude number of the undisturbed flow (Baines (1995) p. 111). For $D/d_l \to 0$ the flow problem can be analyzed with linear theory, while for $D/d_l = 0(1)$ nonlinearities appear in the form of hydraulic jumps and rarefactions. When $d_l/d_u \to 0$, the upper layer of light fluid can be assumed to be stationary. Consequently, the equations of motion for the lower layer resemble those for the problem of a single layer of fluid with a free surface flowing

past bottom topography, but with Earth's gravitational acceleration g replaced with the reduced gravity $g' = g(\rho_l - \rho_u)/\rho_u$. This model is called a $1\frac{1}{2}$-layer model. For $d_l/d_u = O(1)$ the equations of motion for both layers must be considered, so that one obtains a 2-layer model (or $2\frac{1}{2}$-layer model if a free surface above the upper layer is accounted for). The problem of a finite volume gravity current flowing past a surface-mounted obstacle was first studied by Rottman *et al.* (1985) with a $1\frac{1}{2}$-layer model, and later analyzed in more depth by Lane-Serff *et al.* (1995) with both $1\frac{1}{2}$ and 2-layer models, as well as a series of laboratory experiments. The authors focused on a configuration in which the two fluid layers are counter-flowing, so that there is no net flow across a plane perpendicular to the flow direction (Lane-Serff *et al.* (1995)). Co-flowing layers (Baines (1995)) or counter-flowing layers with non-zero net flow (Armi & Farmer (1986); Farmer & Armi (1986)) have been addressed as well.

When a gravity current encounters an obstacle, a portion of the dense fluid flow passes over the obstacle while the rest of the dense fluid flow is reflected in the upstream direction. Considerable attention has been devoted to quantifying the influence of the obstacle height on the over-passing flux (Rottman *et al.* (1985), Lane-Serff *et al.* (1995), and Greenspan & Young (1978) for the classic dam-break problem), and predictions based on steady shallow water theory have been found to agree well with experimental measurements (Lane-Serff *et al.* (1995)). By comparison, less attention has focused on the influence of the obstacle height on the front speed of the gravity current that forms downstream. Predicting this speed is important when the objective of the barrier is to reduce the speed of the oncoming gravity current to protect, for example, submarine installations. Hence, our first objective is to extend the $1\frac{1}{2}$ steady shallow water model of Rottman *et al.* (1985) and Lane-Serff *et al.* (1995), in order to predict the front speed and the height of the current downstream of the obstacle. As a key difference between the present analysis and that of the well-studied problem of a flow of denser fluid under lighter fluid past bottom topography (e.g. Baines (1995)), we will not match the flow conditions far downstream of the obstacle to those far upstream (cf. section 4.3). Throughout the present work, the predictions of the model are compared with results from two-dimensional Navier-Stokes simulations that capture many of the important aspects of the interaction of compositional gravity currents with surface-mounted obstacles (Gonzalez-Juez *et al.* (2008*a*)). To achieve this first objective, simulations of the front speed and height of constant-flux gravity currents or starting plumes (cf. Simpson (1997) p. 176) will be performed.

Recently, the time-varying force on surface-mounted rectangular obstacles from the impact of gravity currents has been investigated both experimentally (Ermanyuk & Gavrilov (2005*b*)) and numerically (Gonzalez-Juez *et al.* (2008*a*)). These studies demonstrate that the magnitude of the drag increases exponentially towards a first maximum when the current impinges on the obstacle, then goes through a transient phase, and finally reaches a quasisteady value. Both experiments and simulations show the drag to reach its maximum during impact, when it can be more than twice as large as during the quasisteady stage. Hence, our second objective is to obtain an estimate of this maximum drag. Since the impact stage cannot be captured with a steady shallow water model, we will have to base this estimate on insight gained from the Navier-Stokes simulations.

Gravity current flows around circular cylinders mounted some distance above a wall have received particular attention. This is motivated by the need to obtain estimates for the time-varying force on submarine pipelines (Ermanyuk & Gavrilov (2005*a*); Gonzalez-Juez *et al.* (2008*b*)). Even though this complex flow problem is not amenable to shallow water analysis, the estimate of the maximum drag for a square ridge provided in the present work can be used as an upper bound for this problem, based on the observations

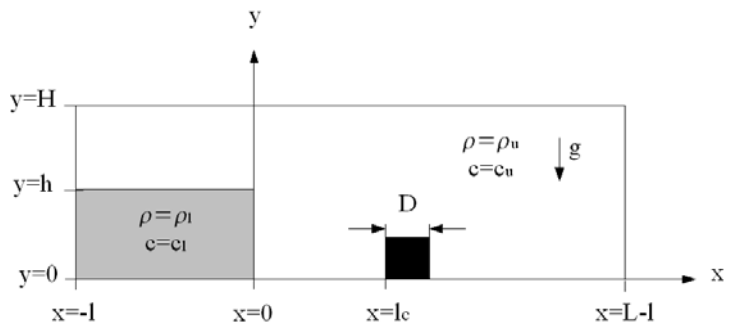

FIGURE 1. Schematic of the flow configuration. A channel of length L and height H contains a lock of length l and height h. When the gate at $x = 0$ is opened, a current of the denser fluid forms and propagates towards a square ridge of side length D, which is situated a distance l_c away from the gate.

that circular cylinders experience the largest drag when they are in contact with the bottom wall (Gonzalez-Juez *et al.* (2008*b*)), and that cylinders with square cross-sections experience larger forces than those with circular cross sections (Gonzalez-Juez *et al.* (2007, 2008*b*)).

The manuscript is organized as follows. Section 2 defines the geometrical set-up of the problem and describes the numerical simulations and parameters considered in this work. A basic description of the flow obtained from the simulations is given in section 3. The shallow water model is described in section 4 and compared with results from simulations in section 5. The estimation of the maximum drag is described in section 6, and comparisons between the predictions of the model and results from the simulations are provided. Finally, section 7 summarizes the main findings and conclusions.

2. Problem description and computational approach

In order to address the objectives outlined above, we conduct two-dimensional numerical simulations of lock-exchange gravity currents interacting with square ridges. These currents are compositional in nature, with the density difference caused by differential concentration fields. Figure 1 shows a sketch of the channel of length L and height H, filled with ambient fluid of density ρ_u and concentration c_u. Submerged in it is a lock of length l and height h, which contains the denser fluid of density ρ_l and concentration c_l. When the vertical gate at $x = 0$ is opened, a current of the denser fluid forms with an approximate thickness of $d = h/2$ (Huppert & Simpson (1980); Shin *et al.* (2004)), and propagates towards the right along the floor of the channel. After traveling a distance l_c, it encounters an obstacle with square cross-section and side length D.

The simulations are based on the dimensionless form of the two-dimensional Navier-Stokes equations in the Boussinesq approximation (Härtel *et al.* (2000); Ooi *et al.* (2005); and others). A characteristic velocity exists in the form of the buoyancy velocity $u_b = \sqrt{g'd}$. The relationship between density and concentration c is assumed to be linear, and given by $\rho = \rho_u + (\rho_l - \rho_u)(c - c_u)/(c_l - c_u)$. By using d as a length-scale, and u_b as a velocity scale, the following dimensionless variables, denoted with asterisks, are defined: $t^* = t/(d/u_b)$, $\mathbf{u}^* = \mathbf{u}/u_b$, $p^* = (p - p_{ref})/(\rho_u u_b^2)$, and $c^* = (c - c_u)/(c_l - c_u)$. Here, $\mathbf{u}$ denotes the velocity vector ($\mathbf{u} = (u, v)$), p the total pressure, and p_{ref} a reference pressure. With this non-dimensionalization, the conservation of mass, momentum, and

concentration takes the form

$$\nabla \cdot \mathbf{u}^* = 0 \,, \tag{2.1}$$

$$\frac{\partial \mathbf{u}^*}{\partial t^*} + \nabla \cdot \mathbf{u}^* \mathbf{u}^* = -\nabla p^* + \frac{1}{Re_d} \nabla^2 \mathbf{u}^* + c^* \mathbf{e}^g \,, \tag{2.2}$$

$$\frac{\partial c^*}{\partial t^*} + \nabla \cdot c^* \mathbf{u}^* = \frac{1}{Re_d \, Sc} \nabla^2 c^* \,, \tag{2.3}$$

where $\mathbf{e}^g$ indicates the unit vector pointing in the direction of gravity.

The dimensionless governing parameters are the Reynolds number $Re_d = u_b d/\nu$ and the Schmidt number $Sc = \nu/\kappa$, where ν represents the kinematic viscosity and κ the molecular diffusivity, respectively.

The bottom ($y = 0$) boundary is treated either as a no-slip or slip wall, while the top ($y = H$) boundary is considered to be a slip wall. The left ($x = -l$) boundary of the computational domain, and the surface of the obstacle, are treated as no-slip boundaries. A convective boundary condition is employed along the right boundary ($x = L - l$) of the domain (Pierce (2001)). The flow field is initialized with the fluid at rest everywhere, and the dimensionless concentration c^* being one (zero) within (outside) the lock.

A well-validated finite-volume code is used in this work (Pierce (2001); Pierce & Moin (2004); Gonzalez-Juez *et al.* (2008*a*)). The momentum and concentration conservation equations are discretized on a non-uniform Cartesian mesh, which is refined close to the bottom wall and close to the obstacle. Time integration is accomplished via an iterative procedure similar to the Crank-Nicolson scheme. To ensure that the continuity equation is satisfied, a Poisson equation for the pressure correction is solved at each time step. The simulation of irregular domains is accomplished by means of a grid blanking methodology. Results obtained with this code closely reproduce the experiments by Ermanyuk & Gavrilov (2005*a*,*b*), cf. Gonzalez-Juez *et al.* (2007, 2008*a*).

The computational domain length is kept at $L/d = 48$ for all simulations. A lock length of $l/d = 18$ ensures that reflections from the left wall do not influence the interaction between the gravity current and the obstacle, during the time of the simulation. The distance between the gate and the obstacle is chosen as $l_c/d = 6$, so that the current is in the constant front speed phase when it encounters the square ridge (Simpson (1997) p. 167). The ratio of the channel height and the lock height is set to $H/h = 5$, which approximates well the deep ambient case of $H/d \to \infty$ found in practice (Gonzalez-Juez *et al.* (2008*a*)). The value for Re_d considered in this work is 707, which is representative of laboratory gravity currents, allows to resolve all the scales of motion with direct numerical simulations, and is sufficiently large for Re_d not to be a dominant parameter of the flow problem; selected data for $Re_d = 3,535$ are also discussed. The Schmidt number Sc is kept at unity.

The side of the square ridge is varied in the range $D/d = 0.3 - 1.6$, which ensures that D/d is sufficiently small not to block the current completely, while being large enough for linear theory to be invalid (Baines (1995) p. 39). For comparison, typical gravity current heights of O(1-100m) and obstacle length scales of $O(1m)$ yield a range of $D/d = 0.01 - 1.0$. A grid of 2,048×320 is employed, along with a time step of $\Delta t/(d/u_b) = 0.003$. The grid spacing near the obstacle is at most $0.02D$.

In the present work, the key control parameters of the simulations hence are the obstacle height or square side D/d and the use of either no-slip or slip bottom boundary conditions. With slip bottom boundaries the retarding effect of the bottom boundary layer is eliminated, producing currents with higher dimensionless front speeds $V/\sqrt{g'd}$ (e.g. Härtel *et al.* (2000)). We remark that two-dimensional simulations will be sufficient

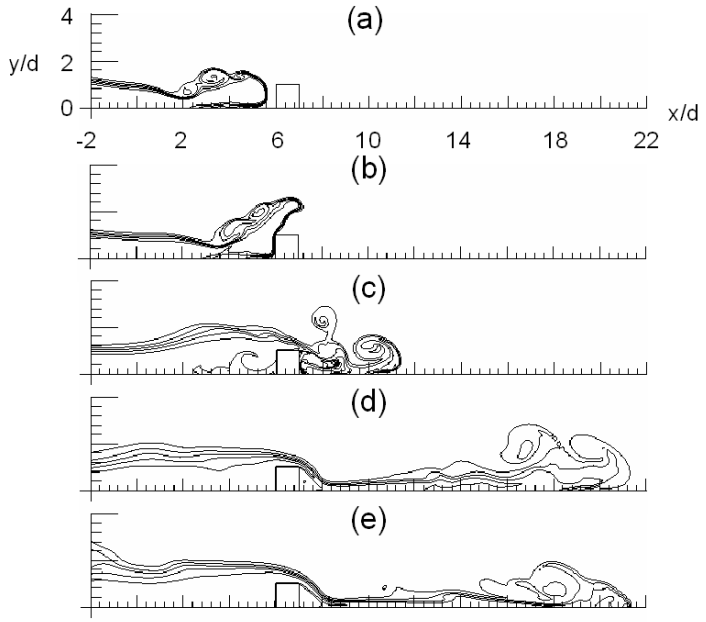

FIGURE 2. Interaction of a gravity current and a square ridge with $D/d = 1$ and a no-slip (a-d) or slip (e) bottom boundary condition. The corresponding times are $t/\sqrt{d/g'} = 7.4$ (a), 9.6 (b), 17.5 (c), 36.2 (d), and 27.7 (e). The current is visualized by means of the $c^* = 0.1$, 0.3, 0.5, 0.7 and 0.9 concentration contours. The current head is deflected upward by the obstacle, overshoots it, and subsequently reestablishes itself downstream of the obstacle. Note that only a fraction of the computational domain is shown.

for the purpose of the present investigation, since our earlier comparison between two- and three-dimensional simulations (Gonzalez-Juez *et al.* (2008*a*)) showed that both the force magnitude during the impact stage and the front velocity during the quasisteady phase are well reproduced in two dimensions.

3. Basic flow description

Figure 2(a-c) shows the evolution of the flow field with time during the impact and transient stages, for $D/d = 1$ and a no-slip bottom boundary, at $Re = 707$. Frames (d) and (e) depict the flow during the quasisteady state ($t/\sqrt{d/g'} > 17$) for both no-slip and slip bottom boundaries, respectively. Upon encountering the obstacle (a), the current head is deflected upward (b), and eventually reattaches downstream of the obstacle (c). Subsequently, the flow around the obstacle reaches a quasisteady state, and the current reestablishes itself downstream of the obstacle (d).

The temporal evolution of the gravity current front position is shown in figure 3 for a no-slip bottom boundary and different values of D/d. Here the current front is defined as the x-location where the height of the dense fluid layer, defined as

$$\frac{d_{x,t}}{d} = \int_0^\infty \left(\frac{c - c_u}{c_l - c_u}\right) d\left(\frac{y}{d}\right) \tag{3.1}$$

has a value $d_{x,t}/d = 10^{-3}$, consistent with the definition employed by Cantero *et al.* (2007). The gravity current speed ($V/\sqrt{g'd}$) is given by the slope of the curves in figure 3. We observe that, after a transient phase lasting until approximately $t/\sqrt{d/g'} \approx 25$,

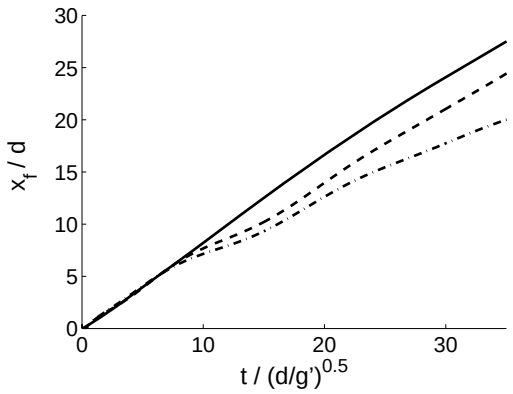

FIGURE 3. Temporal evolution of the gravity current front position (x_f/d) for no-slip bottom boundaries and different obstacle sizes D/d: 0.3 (solid lines), 0.8 (dashed lines), and 1.2 (dash–dotted lines). After a transient phase, the front speed of the current downstream of the obstacle becomes approximately constant. It decreases with increasing obstacle height.

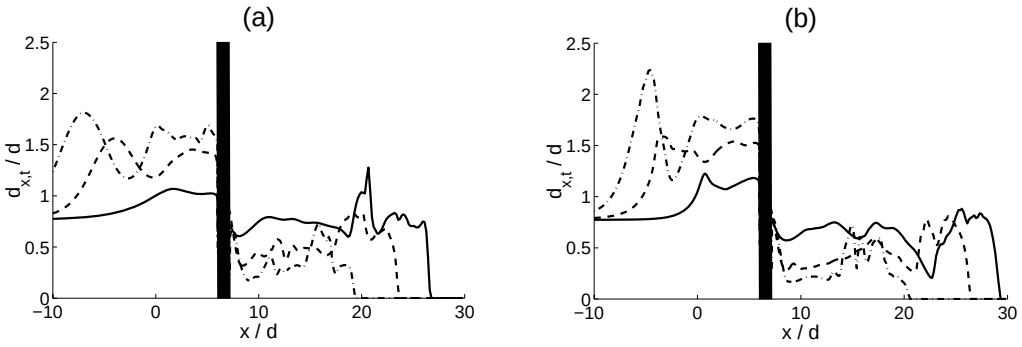

FIGURE 4. Streamwise variation of the current height $d_{x,t}/d$: (a) at $t/\sqrt{d/g'} = 33.9$ for a no-slip bottom wall; and (b) at $t/\sqrt{d/g'} = 31.1$ for a slip bottom wall. The values of D/d are: $D/d = 0.3$ (solid lines), 0.8 (dashed lines), and 1.2 (dash-dotted lines). The obstacle location is denoted with a thick vertical line. Note that the height of the current forming downstream of the obstacle decreases with increasing obstacle height D/d. The streamwise variation of $d_{x,t}/d$ upstream of the obstacle indicates the presence of a hydraulic jump.

the front speed of the current downstream of the obstacle assumes a roughly constant value that decreases with increasing obstacle size.

Figure 4 displays the streamwise variation of the current height $d_{x,t}/d$ for different obstacle sizes D/d and both no-slip (a) and slip (b) bottom boundaries. Note that the height of the current forming downstream of the obstacle decreases with increasing obstacle size D/d. Similar findings were observed for other sets of parameters.

As explained above, one of our objectives is the development of a model for the prediction of the speed and height of the current downstream of the obstacle. This model, which extends the earlier work by Rottman *et al.* (1985) and Lane-Serff *et al.* (1995), will be described in the following.

4. Shallow water model

The gravity current flow over the obstacle during the quasisteady state, cf. figures 2d and 2e, can be divided into a dense fluid layer at the bottom, and a light fluid layer on top.

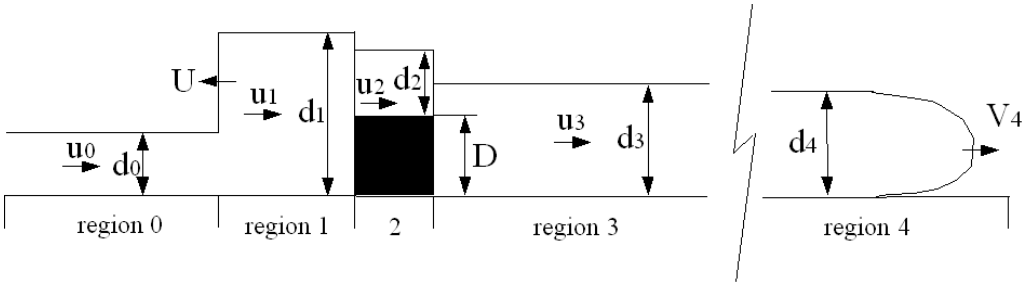

FIGURE 5. Schematic showing a gravity current flowing past an obstacle during the quasisteady state. The present analysis divides the flow into five distinct regions.

We assume inviscid Boussinesq flow with a rigid top wall, along with negligible mixing between the layers. For the values of H/h considered in this work, the simulations show that the horizontal velocities in the upper layer are small compared to those in the lower layer, so that a $1\frac{1}{2}$-layer model can be used. The flow is divided into five distinct regions, as shown in figure 5: the inflow region (0), the region between the reflected flow structure and the obstacle (1), the region at the obstacle location (2), the region immediately downstream of the obstacle (3), and the head of the gravity current downstream of the obstacle (4). We employ subscripts to denote the horizontal velocity u, the layer height d, the flux $q = ud$, and the Froude number $Fr = u/\sqrt{g'd}$ in each region.

For the shallow water model, the current height in the inflow region d_0 and $\sqrt{g'd_0}$ are chosen as the length and velocity scales. This is in contrast to the nondimensionalization employed for the simulation work, where we employed the half-height d of the lock and $\sqrt{g'd}$, since they are the only quantities known a priori. Two governing dimensionless parameters exist in the form of the ratio of the obstacle height and the height of the dense fluid layer of the inflow region, D/d_0, and the inflow Froude number $Fr_0 = u_0/\sqrt{g'd_0}$. Following Lane-Serff *et al.* (1995), for the purpose of comparing with simulation results we will later set u_0 equal to the front speed of the lock-exchange gravity current, and d_0 equal to the thickness of the undisturbed tail of this current. As will be discussed in more detail in section 5, for the parameter range typically considered here the inflow Froude number is subcritical ($Fr_0 < 1$) in currents with no-slip bottom boundaries, whereas it is supercritical ($Fr_0 > 1$) in currents with slip bottom boundaries.

4.1. *Region upstream of the obstacle*

Figure 2c indicates the presence of a hydraulic jump some distance upstream of the obstacle. This is confirmed by the streamwise profile of $d_{x,t}/d$ in figure 4. A detailed inspection of the simulation results furthermore shows this jump to move upstream. Figure 4 also demonstrates that the variation of $d_{x,t}/d$ upstream of the obstacle is smoother for the slower current with no-slip boundaries, suggesting the presence of a smooth or undular jump with subcritical inflow conditions. By comparison, $d_{x,t}/d$ varies more abruptly for the faster current with slip boundaries, indicating the presence of a strong jump. No rarefactions were detected in the reflected structure. Thus, for the purpose of developing a model, we assume that upstream of the obstacle a reflected hydraulic jump or internal bore exists that moves upstream with a constant speed U.

After changing to a reference frame moving with the jump sped U, conservation of mass and momentum across the jump give

$$(u_0 - U)d_0 = (u_1 - U)d_1\,, \tag{4.1}$$

$$\frac{1}{2}g'd_0^2 + (u_0 - U)^2 d_0 = \frac{1}{2}g'd_1^2 + (u_1 - U)^2 d_1 \,. \tag{4.2}$$

Furthermore, conservation of mass at the obstacle, between regions 1 and 2, yields

$$u_1 d_1 = u_2 d_2 \,. \tag{4.3}$$

By following the approach of Lane-Serff *et al.* (1995) and applying Bernoulli's principle between regions 1 and 2, we obtain

$$\frac{1}{2}u_1^2 + g'd_1 = \frac{1}{2}u_2^2 + g'(d_2 + D) \,. \tag{4.4}$$

Note that Rottman *et al.* (1985) proceed differently at this juncture, by replacing equation (4.4) with the assumption $d_2 = d_1 - D$.

4.2. *The obstacle location*

Figure 6 shows the streamwise variation of the Froude number $Fr_{x,t}$ for different values of D/d. Here, $Fr_{x,t}$ is defined as

$$Fr_{x,t} = \frac{q_{x,t}}{\sqrt{g'd_{x,t}^3}} \,, \tag{4.5}$$

with the flux of dense fluid per unit width across an x-plane given by

$$\frac{q_{x,t}}{\sqrt{g'd^3}} = \int_0^\infty \left(\frac{c - c_u}{c_l - c_u}\right)\left(\frac{u}{\sqrt{g'd}}\right) d\left(\frac{y}{d}\right) \,. \tag{4.6}$$

We consistently find an abrupt streamwise variation of $Fr_{x,t}$ at the obstacle location, where the critical condition $Fr_{x,t} = 1$ is reached for $D/d \geqslant 0.5$. For $D/d < 0.5$, the criticality can still be achieved some distance downstream of the obstacle, cf. figure 6. For the purpose of developing a simplified flow model, we assume criticality at the obstacle location

$$\frac{u_2}{\sqrt{g'd_2}} = 1 \,. \tag{4.7}$$

Note that assuming a hydraulically controlled obstruction is common in the modeling of single- and two-layer flows past bottom topography (e.g. Rottman *et al.* (1985), Lane-Serff *et al.* (1995), Woods *et al.* (1998) and Oehy & Schleiss (2007) for gravity current flows; Armi & Farmer (1986) and Farmer & Armi (1986) for exchange flows; and Baines (1995) p. 38-40 for single layer flows).

4.3. *Regions downstream of the obstacle*

In order to be able to relate the properties of the current downstream of the obstacle to the upstream flow conditions, we will now extend the approach taken by Rottman *et al.* (1985) and Lane-Serff *et al.* (1995), and consider regions 3 and 4, cf. figure 5. Figure 6 shows that for all but the smallest obstacles the flow reaches a supercritical state ($Fr_{x,t} > 1$) downstream of the obstacle. Even further downstream, a super- to subcritical transition occurs for the slower current with a no-slip bottom wall, whereas the flow remains mostly supercritical for the faster current with a slip wall. In the terminology of Baines (1995) (his figures 2.9 and 2.11), we observe a partially blocked flow with a lee jump for a no-slip bottom wall, and a flow without lee jump for a slip wall. The

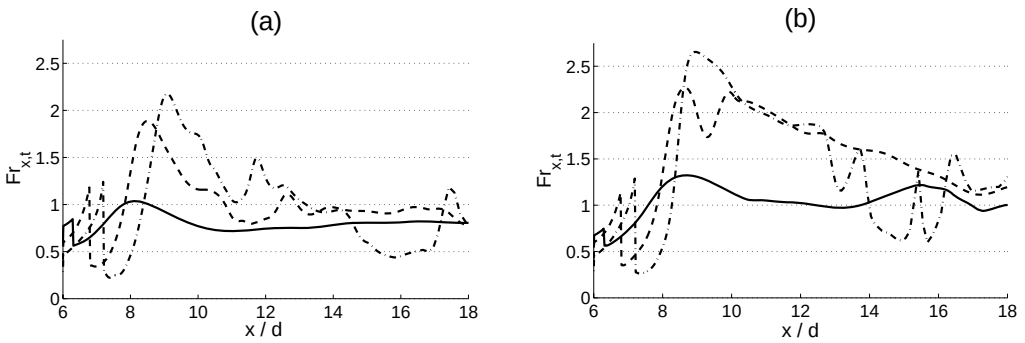

FIGURE 6. Streamwise variation of $Fr_{x,t}$ downstream of the obstacle: (a) at $t/\sqrt{d/g'} = 33.9$ for a no-slip bottom wall; and (b) at $t/\sqrt{d/g'} = 31.1$ for a slip bottom wall. The different obstacle sizes D/d are: $D/d = 0.3$ (solid lines), 0.8 (dashed lines) and 1.2 (dash-dotted lines). The upstream face of the obstacle is located at $x/d = 6$. The flow reaches a critical state near the obstacle. Further downstream (near $x/d = 11$ for $D/d = 0.8$, and near $x/d = 13$ for $D/d = 1.2$), a super- to subcritical transition occurs for subcritical inflow conditions and a no-slip bottom wall. For supercritical inflow conditions and a slip wall, the flow remains mostly supercritical.

simulations show that the lee jump, when present, is smooth, of small amplitude, and stationary. Note that, in contrast, figure 2.12 in Baines (1995) predicts a strong lee jump with noticeable speed (of about $0.2\sqrt{g'd_0}$) for the values of Fr_0 and D/d_0 considered here. This discrepancy stems from the fact that in Baines (1995) the flow structures (jumps and/or rarefactions) downstream of the obstacle are constructed such that $V_4 = V_0$ and $d_4 = d_0$, which does not apply to the present case, cf. figures 3 and 4.

The fact that the lee jump, if present, is stationary has two implications. First, the flux at the obstacle equals the flux supplied to the current downstream

$$q_2 = q_4\,, \quad \text{i.e.} \quad u_2 d_2 = u_4 d_4\,. \tag{4.8}$$

This is confirmed by the simulations: Figure 7 shows that for each value of D/d the flux $q_{x,t}/(g'd^3)^{0.5}$ is approximately constant with x between the obstacle and some distance upstream of the current head. Only in the immediate neighborhood of the head do we observe more substantial variations of the instantaneous flux, as a result of unsteady dynamics. Moreover, figure 8 shows that this flux remains approximately constant with time at the obstacle ($x/d = 6$) during the quasisteady period. Furthermore, the lee jump, if present, does not catch up with the front of the downstream current, implying that the front conditions of the current are independent of the events at the obstacle location. As a consequence of these two observations, detailed information about the transition from region 3 to region 4 is not required to determine the speed and the height of the front. Rather, it suffices to know that $q_2 = q_3 = q_4$. In fact, region 3 could be eliminated altogether for the purpose of determining the front properties. Nevertheless, we do keep region 3 in our consideration, in order to be consistent with previous work (Baines (1995)).

At this point, with Fr_0 and D/d_0 given, the five equations (4.1)-(4.4) and (4.7) can be solved iteratively for the five unknowns u_1, d_1, U, u_2, and d_2. Furthermore, we have made the observation that the flux passing over the obstacle ($q_2 = u_2 d_2$) approximately equals the flux near the head of the current ($q_4 = u_4 d_4$), cf. equation (4.8). However, equations (4.1)-(4.4), (4.7), and (4.8) do not suffice for determining both the speed u_4 and the height d_4 of the gravity current downstream of the obstacle. In order to close the system of equations, we require one additional relationship. In this regard, the observation of an

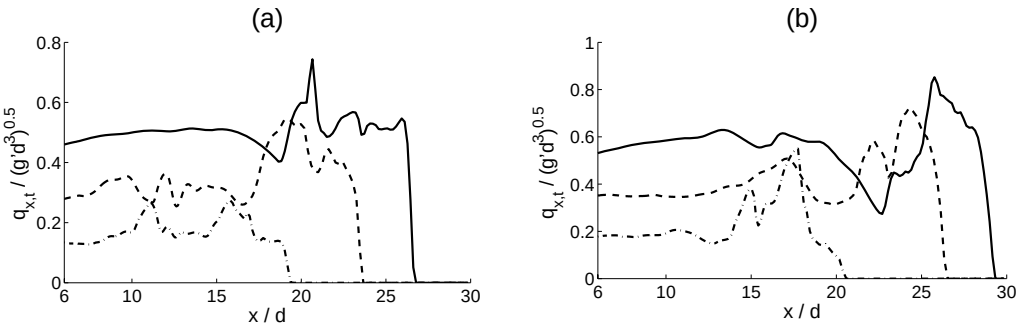

FIGURE 7. Streamwise variation of $q_{x,t}/\sqrt{g'd^3}$ downstream of the obstacle: (a) at $t/\sqrt{d/g'} = 33.9$ for a no-slip bottom wall; and (b) at $t/\sqrt{d/g'} = 31.1$ for a slip bottom wall. The different obstacle sizes D/d are: $D/d = 0.3$ (solid lines), 0.8 (dashed lines) and 1.2 (dash-dotted lines). The upstream face of the obstacle is located at $x/d = 6$. The flux is approximately constant from the obstacle to the neighborhood of the current head far downstream of the obstacle, i.e. $q_2 = q_4$ and $u_2 d_2 = u_4 d_4$.

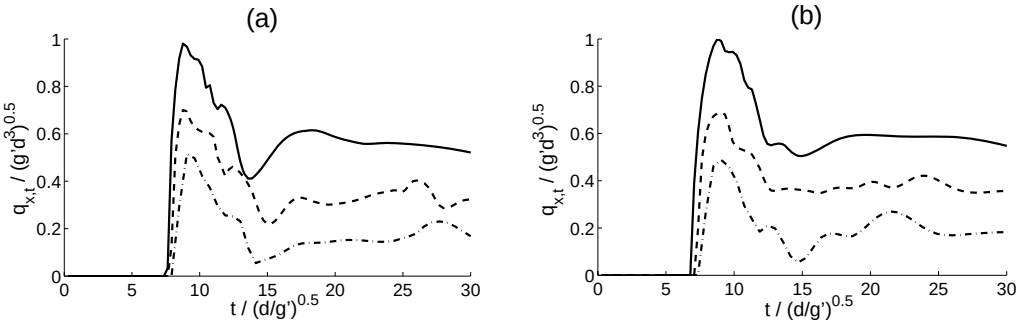

FIGURE 8. Temporal variation of $q_{x,t}/\sqrt{g'd^3}$ at the obstacle location ($x/d = 6$) for no-slip (a) and slip (b) bottom boundaries, and for different obstacle sizes D/d: $D/d = 0.3$ (solid lines), 0.8 (dashed lines) and 1.2 (dash-dotted lines). Note that beyond the impact stage, the flux remains approximately constant with time during the quasisteady stage.

approximately constant flux with time in the Navier-Stokes simulations suggests that we take a closer look at the relationship between front velocity and thickness for constant flux currents.

4.4. *Constant-flux gravity currents*

Consider a rectangular channel of length L and height H, in which a denser fluid is being injected into a quiescent ambient fluid through a slot of height $d \ll H$, cf. figure 9. Note that the slot height in this flow in a sense corresponds to half the lock height in the problem described in section 2, as both represent approximate measures of the gravity current height. We assume the inlet velocity V_{in} to be constant across the slot. The flow that forms some distance downstream from the inlet is referred to as a constant-flux gravity current or starting plume. We neglect the entrainment of ambient fluid, so that the volume flux per unit width $q = dV_{in}$ is preserved downstream. The momentum flux, on the other hand, varies in the streamwise direction, as it is affected by the horizontal gradient of the hydrostatic pressure. Didden & Maxworthy (1982) analyzed such flows and showed that, when gravitational and inertial forces are in balance (Simpson (1997)), their front velocity V_{cf} and thickness d_{cf} follow the relationships

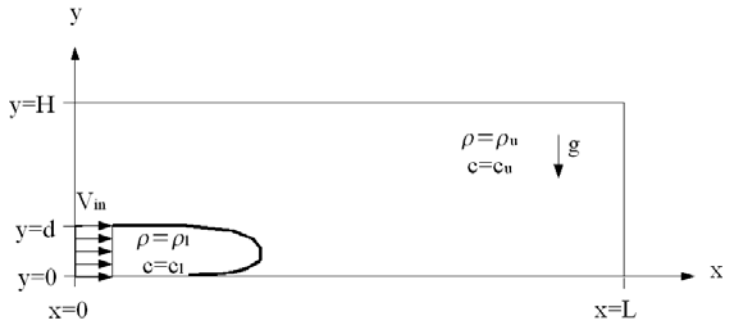

FIGURE 9. Schematic of the flow configuration for constant-flux gravity current simulations. A denser fluid is injected through a slot of height d into a rectangular channel of length L and height H containing a quiescent ambient fluid.

$$V_{cf} = C(g'q)^{1/3} \ , \tag{4.9}$$

$$d_{cf} = \frac{1}{C}\left(\frac{q^2}{g'}\right)^{1/3} \ . \tag{4.10}$$

The inviscid theory of Benjamin (1968), based on Bernoulli's principle, yields $Fr = V_{cf}/\sqrt{g'd_{cf}} = \sqrt{2}$ and $C = 2^{1/3}$.

4.5. *Model predictions*

We can now compute the front speed $V_4/\sqrt{g'd_0}$ and thickness d_4/d_0 of partially obstructed currents as functions of D/d_0 and Fr_0. To do so, we close the system of equations given by (4.1)-(4.4), (4.7) and (4.8) with equations (4.9) and (4.10). This approach holds for partially obstructed currents whose front speed is constant with time, i.e., governed by a balance of gravitational and inertial forces (Simpson (1997)). Initially, we will employ Benjamin's value for C Benjamin (1968). Further below, we will also explore the strategy of employing empirical values for C obtained from simulations, in order to improve the accuracy of the model predictions.

For $C = 2^{1/3}$, the model predictions for the flux $q_4/\sqrt{g'd_0^3}$, front speed $V_4/\sqrt{g'd_0}$ and thickness d_4/d_0 of the gravity current downstream of the obstacle are shown in figures 10 and 11. Figure 10 shows a noticeable decrease of the flux as the obstacle height increases. This reduced flux renders the downstream current both slower and thinner, as shown in figure 11, consistent with equations (4.9) and (4.10). Note in figure 11b that the decrease of d_4/d_0 with D/d_0 is approximately linear.

5. Comparison of model predictions and Navier-Stokes simulations

For the purpose of comparing predictions of the above model with Navier-Stokes simulation results, we set u_0 and d_0 equal to the front speed V and thickness of the oncoming current, respectively. These quantities are obtained from simulations of unobstructed gravity currents as follows. The current front speed $V/\sqrt{g'd}$ is calculated as described in section 3, while the thickness d_0 is evaluated by spatially averaging $d_{x,t}$ from $x = 0$ to the front location $x = x_f$. For $Re = 707$ and $H/h = 5$, we find $V/\sqrt{g'd} = 0.83$ (1.00) for no-slip (slip) bottom boundaries. This result for the slip bottom is within 5% of the relationship $V/\sqrt{g'd} = (1 - d/H)^{0.5}$ given by Shin *et al.* (2004). Furthermore, we observe $d_0/d = 0.88$ (0.82) for no-slip (slip) bottom walls. Hence, for the Froude

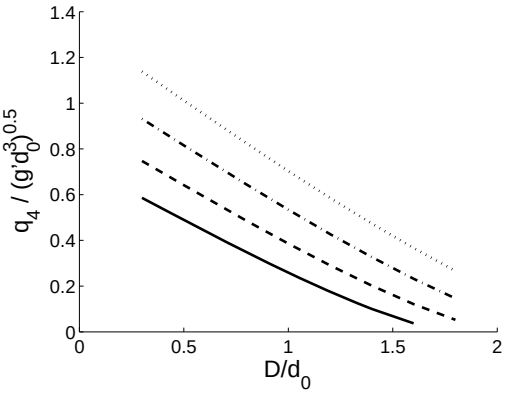

FIGURE 10. Effect of D/d_0 on the over-passing flux $q_4/\sqrt{g'd_0^3}$ of partially obstructed currents for different values of Fr_0: 0.7 (solid line), 0.9 (dashed line), 1.1 (dashed-dotted line), and 1.3 (dotted line).

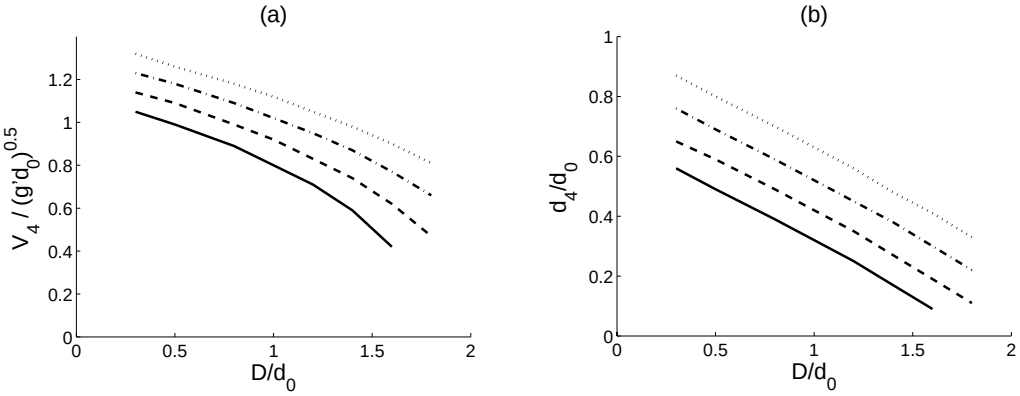

FIGURE 11. Effect of D/d_0: (a) on the front speed $V_4/\sqrt{g'd_0}$; and (b) on the thickness d_4/d_0 of partially obstructed currents for different values of Fr_0: 0.7 (solid line), 0.9 (dashed line), 1.1 (dashed-dotted line), and 1.3 (dotted line). Results using the shallow water model with Benjamin's value $C = 2^{1/3}$ are shown. The isolated obstacle reduces the speed and height of the downstream gravity current by reducing its flux.

number $Fr_0 = u_0/\sqrt{g'd_0}$ of the unobstructed current we obtain $Fr_0 = 0.88$ (1.11) for no-slip (slip) bottom walls. By comparison, past experiments show $Fr_0 = 0.86 - 1.08$ for $H/h \approx 5$, though d_0 is defined in different ways (using the data of figures 13 and 14 for $H/h = 0.17$ in Shin *et al.* (2004) and equation (2.1) of Huppert & Simpson (1980)). Note that for a no-slip bottom the inflow conditions are subcritical ($Fr_0 < 1$), while for a slip bottom they are supercritical ($Fr_0 > 1$).

The front speed V_4 of the gravity current downstream of the obstacle is calculated by tracking the front of the current, as described in section 3, over a time interval during which the speed is seen to be approximately constant. The height d_4 of this current is found by spatially averaging $d_{x,t}$ from $x/d = 10$ to the front, at a time when it is located near the end of the computational domain ($x/d \approx 44$).

Figure 12 compares model predictions (employing the Benjamin value of $C = 2^{1/3}$) and Navier-Stokes simulation results for the influence of D/d_0 on $V_4/\sqrt{g'd_0}$ and d_4/d_0. While most of the simulation data are for $Re_d = 707$, a few data for $Re_d = 3,535$ are included for no-slip boundaries. Overall, for no-slip boundaries the current velocity

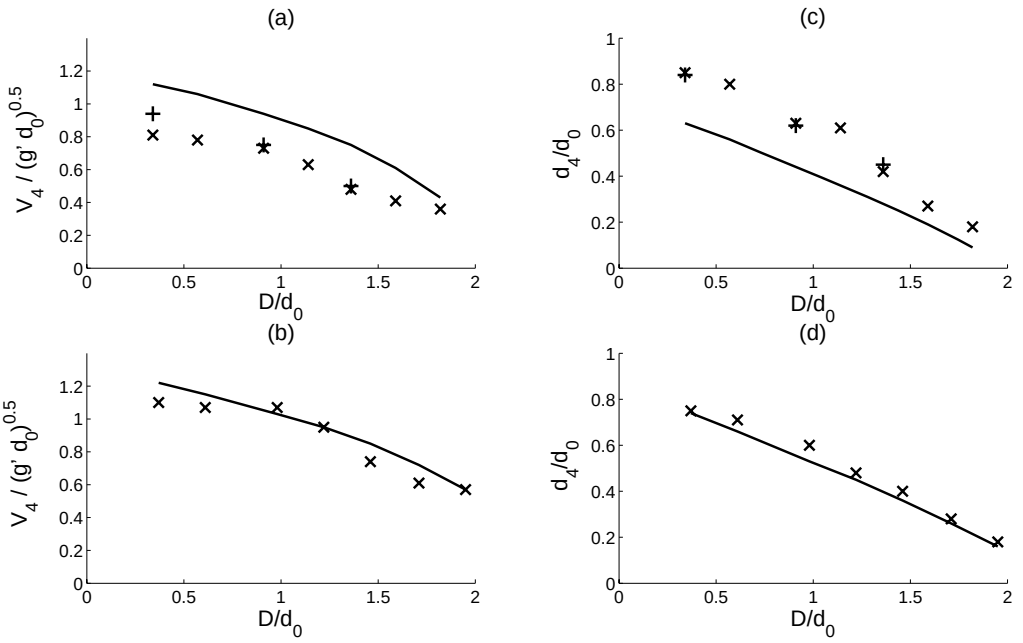

FIGURE 12. Effect of D/d_0 on the front speed $V_4/\sqrt{g'd_0}$ (a and b) and thickness d_4/d_0 (c and d) of partially obstructed currents with no-slip (a and c) or slip (b and d) bottom boundaries. Results using the shallow water model with Benjamin's value for C are shown (solid lines), along with results from the simulations at $Re_d = 707$ (crosses) and $Re_d = 3,535$ (plus signs). For slip walls, we observe good agreement between the model prediction and the simulation results, whereas for no-slip walls the model overpredicts (underpredicts) the velocity (height) of the current.

is overpredicted by about 40%, while the height is underpredicted by about 30%. The slightly larger values of $V_4/\sqrt{g'd_0}$, and smaller values of d_4/d_0, for the larger Re_d reflect the larger value of $Fr_0 = 0.93$ at $Re_d = 3,535$, as compared to 0.88 at $Re_d = 707$. In general, the model predictions do not improve notably by increasing Re_d from 707 to 3,535. On the other hand, for slip boundaries the model predictions agree closely with the Navier-Stokes results over the entire range of obstacle heights. In summary, the inviscid model predicts the speed and height of the downstream current quite accurately for slip boundaries, whereas substantial discrepancies are observed for the case of no-slip boundaries.

We now explore the idea of improving the model predictions for no-slip boundaries by employing empirical values of C, in place of Benjamin's value of $2^{1/3}$. Towards this end, we conducted a series of Navier-Stokes simulations of constant flux currents in order to determine C-values for a variety of different flow conditions.

The computational approach is similar to that explained in section 2, with the following differences. The flow configuration used is that shown in figure 9. The slot width d is now used as the length scale, and the buoyancy velocity $\sqrt{g'd}$ as the velocity scale. At the left boundary ($x = 0$), a uniform inflow is prescribed for $0 < y < d$, while the region $d < y < H$ is treated as a no-slip wall. The length and height of the computational domain are $L/d = 40$ and $H/d = 10$, respectively. The following values for the independent parameters Re_d and $V_{in}/\sqrt{g'd}$ are considered: $Re_d = 100$, 707, 1,000, and 10,000, and $V_{in}/\sqrt{g'd} = 0.625$, 1, and 1.2. Note that the inflow velocity is varied to consider both sub- and supercritical inlet conditions. Furthermore, both no-slip and slip bottom boundary

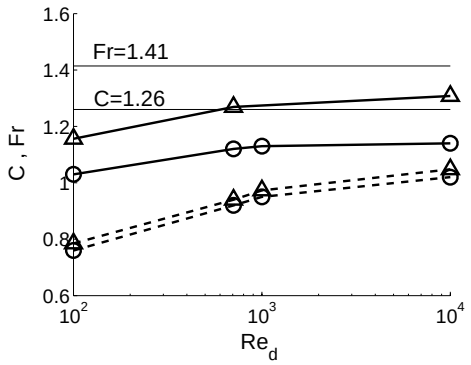

FIGURE 13. Effect of Re_d on C (circles) and Fr (triangles) of constant-flux gravity currents with no-slip (dashed lines) and slip (solid lines) bottom boundaries for $V_{in}/\sqrt{g'd} = 0.625$. The theoretical values for C and Fr by Benjamin (1968) are also indicated. The values for C and Fr found here are consistent with previous theoretical and experimental findings.

conditions are considered. The front speed is calculated by tracking the front of the current, as described in section 3, and d_{cf} is found by averaging $d_{x,t}$ from $x/d = 5$ to the front position at $t/\sqrt{d/g'} = 24$.

For the parameter range investigated, the effect of $V_{in}/\sqrt{g'd}$ on C and Fr was observed to be less than 2%, so that it could be neglected. For $V_{in}/\sqrt{g'd} = 0.625$, figure 13 shows the effect of Re on C and Fr, for both no-slip and slip bottom boundaries. For $Re_d \geqslant 707$ and a slip bottom boundary, the values of C and Fr are within 10% of those given by Benjamin's theory. The difference between the theoretical and simulation results can be attributed to the finite values of Re_d and H/d in the simulations, while these parameters are infinite in Benjamin's theory. For no-slip bottom boundaries, the values of C and Fr obtained from the simulations are consistent with experimental observations for $Re_d = O(10^3)$ and higher, where Keulegan (1958) and Wood (1966) found $C = 1.06$ and $Fr = 1.07 - 1.09$. They also agree with experiments for $Re_d = O(10^2)$ and less, for which Braucher (1950), Britter & Linden (1980) and Hogg *et al.* (2005) measured $C = 0.65 - 0.9$ and $Fr = 0.8 - 0.9$ (cf. the data given in Britter & Linden (1980) for a zero slope, and in Hogg *et al.* (2005) from their experiments 5, 7-9, 16 and 20 for vanishing ambient flow and a source of saline fluid.)

As a next step, we calculate values of C and Fr_4 for currents forming downstream of obstacles, using simulation data for V_4, d_4, and q_4. The effect of D/d_0 on C and Fr is observed to be small, and does not follow any trend. This is notable, since at large values of D/d_0 the current can be considerably distorted, cf. figure 4. More importantly, the mean values of C and Fr, as D/d_0 is varied, are close to those given by simulations of constant-flux currents at the same Re_d ($Re_d = 707$), cf. table 1. This observation further supports the approach of modeling the current downstream of the obstacle as a constant flux current.

We note that the uncertainties in calculating V_4, d_4 and q_4 enter into the final calculation of C and Fr. These uncertainties result from the choice of intervals over which spatial and temporal averages are taken, and they may explain the small difference of the C and Fr-values for constant-flux and partially obstructed currents shown in table 1. Furthermore, the lower Fr seen in partially obstructed currents with no-slip bottom boundaries may to some extent be due to the smaller thickness d_4/d_0 seen in these currents, for which the retarding effect of friction becomes more important.

	C	Fr
no slip, constant-flux	0.92	0.94
no slip, partially obstructed	0.92	0.85
slip, constant-flux	1.12	1.27
slip, partially obstructed	1.22	1.26
Benjamin (1968)	1.26	1.41

TABLE 1. Comparison of the values for C and Fr obtained from Navier-Stokes simulations of constant-flux and partially obstructed currents, respectively, with either no-slip or slip bottom boundary conditions at $Re_d = 707$. Partially obstructed and constant-flux gravity currents are seen to give rise to approximately identical values of C and Fr, which confirms that the former can be treated as constant-flux currents in the present analysis.

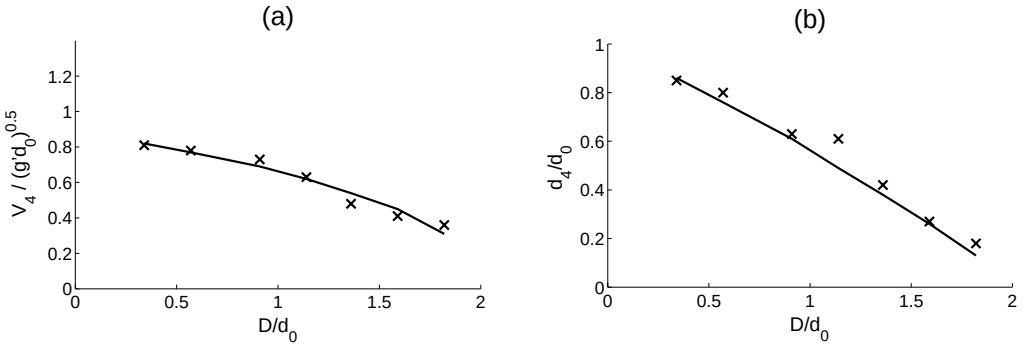

FIGURE 14. Effect of D/d_0 on the front speed $V_4/\sqrt{g'd_0}$ (a) and thickness d_4/d_0 (b) of partially obstructed currents with no-slip bottom boundaries. Model results using empirical values for C are shown (solid lines), along with results from the simulations at $Re_d = 707$ (crosses). The value for C employed is 0.92 and corresponds to that found for constant-flux gravity currents at $Re_d = 707$, cf. table 1. By selecting a value of C of 0.92 instead of $2^{1/3}$ (cf. table 1), which reflects the effect of bottom friction, the model predictions for no-slip currents improve notably.

By selecting a value of C of 0.92 instead of $2^{1/3}$ (cf. table 1), which reflects the effect of bottom friction, the model predictions for no-slip currents improve notably, cf. figure 14. We note that employing Fr_0-values from Shin *et al.* (2004), rather than from simulations of unobstructed currents, generally leads to good agreement with the simulation results as well, although the discrepancy is somewhat larger than that in figures 12 and 14, especially for d_4/d_0.

To conclude, for slip bottom boundaries Benjamin's theoretical C-value results in accurate predictions of both the velocity and the height of the current downstream of the obstacle. On the other hand, for no-slip boundaries and the values for Re_d considered here, an empirical value for C leads to a substantially more accurate prediction. Alternatively, in order to avoid the use of an empirical C-value, a semi-empirical theory could be developed along the lines of Ermanyuk & Gavrilov (2007), taking into account frictional losses. Such objective is, however, outside the scope of the present work. Besides, at very large Re_d the values for C and Fr for no-slip boundaries are expected to approach those for slip boundaries.

Figure 14 shows that both $V_4/\sqrt{g'd_0}$ and d_4/d_0 decrease with D/d_0, and that, as expected, currents flowing over a no-slip bottom wall are slower than those flowing over

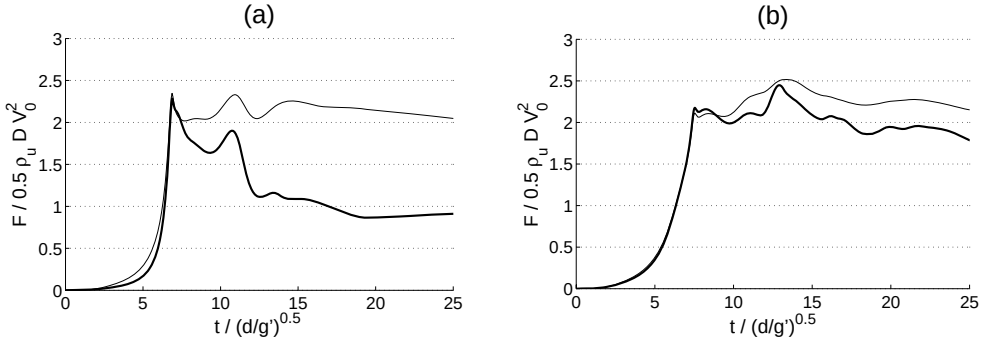

FIGURE 15. Temporal evolution of the drag F_D (thick solid lines) and the pressure force on the obstacle upstream face F_w (thin solid lines) for $D/d = 0.3$ (a) and $D/d = 1.2$ (b), with slip bottom boundaries. The maximum drag approximately equals the maximum value of F_w, and hence is not affected by the wake drag. Furthermore, the value of F_w during the quasisteady state ($t/(d/g') > 17$) approximately equals that at the time of the first maximum drag. This observation allows us to use steady shallow water theory to obtain, indirectly, an estimate for the maximum drag.

a slip wall. The good agreement shown in figure 14 between the simulation results and the predictions from the theory indicates that the isolated obstacle reduces the speed and height of the current downstream of the obstacle by reducing its flux.

The effect of the obstacle on the mixing processes at the interface of the gravity current can be recognized to some extent in figure 2. We note that the concentration contours for the current downstream of the obstacle (figure 2d) are generally spaced farther apart than for the incoming current upstream of the obstacle (figure 2a). This wider spacing of the concentration contours indicates that the downstream current is more diluted. In spite of the fact that our model neglects any mixing between the fluids, its predictions for the front speed height are fairly accurate. Hence we conclude that the effect of mixing on those quantities is small for the parameters considered here.

6. Estimate of the maximum drag

For small viscous forces (Gonzalez-Juez *et al.* (2008*a*)), the overall flow force on the obstacle can be obtained with good accuracy by integrating the pressure distribution over the obstacle surface. The drag F_D represents the streamwise component of this flow force. Figure 15 shows the temporal evolution of the drag for two values of D/d, and for slip bottom boundaries. After increasing exponentially towards a first maximum, the drag fluctuates for a while, and eventually settles around a quasisteady value. Also shown in figure 15 is the temporal evolution of the pressure force F_w on the upstream face. A number of similar simulations for both no-slip and slip boundary conditions show that for $D/d < 1.2$ the drag reaches a maximum when the current first meets the obstacle, while for $D/d \geqslant 1.2$ the drag maximum typically occurs when the bore is being reflected upstream.

Figure 15 shows that the maximum drag approximately equals the maximum value of F_w, which indicates that the maximum drag is determined by the level of hydrostatic pressure upstream of the obstacle and by the deceleration of fluid as it encounters the obstacle. At the same time, the contribution to the maximum drag from the formation of a wake is small, cf. also Gonzalez-Juez *et al.* (2008*a*). The negligible influence of the wake drag on the overall drag maximum suggests that hydraulic theory can be employed for estimating the maximum drag. We furthermore note that no waves are observed at

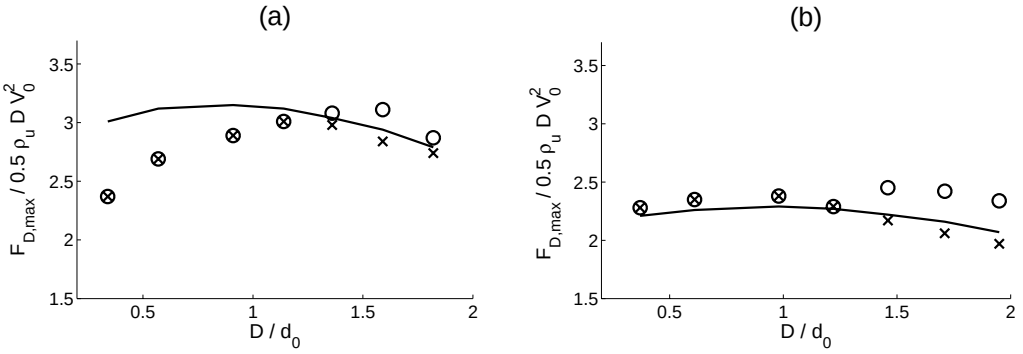

FIGURE 16. Effect of D/d_0 on the first drag maximum (crosses) and the overall drag maximum (circles), from Navier-Stokes simulations. Corresponding shallow water estimates of the drag maximum are indicated by solid lines. Data are provided for both no-slip (a) and slip (b) bottom boundaries. The theoretical estimate is seen to be close to the simulation data for the maximum drag, as long as the obstacle height is much larger than the thickness of the boundary layer at the bottom wall.

the interface between the current and the ambient fluid, so that the wave component of the drag is negligible.

The impact of the current on the obstacle may be modeled with *unsteady* hydraulic theory, by combining the ideas in Greenspan & Young (1978) and Rottman & Simpson (1983) for example, but this would require the numerical solution of the nonlinear shallow water equations, and the resulting numerical model would be considerably less accurate than that described in section 2. For the purpose of obtaining an estimate of the maximum drag, the use of unsteady hydraulic theory can be circumvented by noting in figure 15 that the quasisteady value of F_w approximately equals the drag maximum. This holds both for small obstacles with $D/d < 1.2$, when the drag maximum is reached during the impact stage, and for larger obstacles with $D/d \geqslant 1.2$, where the drag maximum is reached later, but still lies within 15% of the quasisteady value of F_w. These observations result from the rather constant value of d_1 throughout the interaction (also observed by Rottman *et al.* (1985)), except during a transient period after impact. They suggest that the pressure force on the upstream face of the obstacle calculated with *steady* hydraulic theory could be used to accurately estimate the first drag maximum, and with some loss of accuracy, also the overall drag maximum for obstacles with $D/d \geqslant 1.2$. We note that these observations hold for the entire parameter range considered in this work.

To calculate the quasisteady value of F_w, we supplement equations (4.1)-(4.4) and (4.7) by the conservation of momentum between regions 1 and 2

$$\frac{1}{2}g'd_1^2 + u_1^2 d_1 = \frac{1}{2}g'd_2^2 + u_2^2 d_2 + \frac{F_w}{\rho_u}\,. \tag{6.1}$$

The estimate of the maximum drag using the above relation for both no-slip and slip bottom boundaries is shown in figure 16. The largest discrepancy between this estimate and results from numerical simulations occurs for small obstacles and no-slip walls, when the ratio of boundary layer thickness to obstacle height is $O(1)$. Larger obstacles are increasingly exposed to the higher velocity outside the boundary layer (Gonzalez-Juez *et al.* (2008*a*)), and the maximum drag estimate becomes increasingly more accurate. For flows with slip boundaries the maximum drag estimate is reasonably accurate for all obstacle sizes, with the largest discrepancy of $O(10\%)$. Note that the model provides

a better estimate for the first drag maximum than the overall drag maximum, as the former is more closely approximated by F_w during the quasisteady state, cf. above.

7. Summary and Conclusions

In summary, we consider the problem of a partial-depth lock-exchange gravity current flowing past an isolated surface-mounted obstacle. For such partially obstructed gravity currents we extend the steady shallow water models of Lane-Serff *et al.* (1995) and Rottman *et al.* (1985), in order to predict the height d_4 and constant front speed V_4 of the current downstream of the obstacle, along with the maximum drag. The model predictions for these quantities as functions of the Froude number Fr_0 of the oncoming current, and of the ratio D/d_0 of obstacle to current height, are compared with two-dimensional direct numerical simulations.

Based on observations from simulations of partially obstructed and constant-flux gravity currents, we treat the current downstream of the obstacle as a constant-flux current whose flux q_4 equals the flux passing over the obstacle. We calculate this flux from the shallow water model, and subsequently use both theoretical (Benjamin (1968)) and empirical values for $C = V_4/(g'q_4)^{1/3}$, in order to predict the front speed and height of the downstream current. For Benjamin's value of C the model predictions agree well with results from slip wall simulations. On the other hand, for no-slip walls, empirical values of C substantially improve the agreement between model and simulation data. As D/d_0 increases, $V_4/\sqrt{g'd_0}$ and d_4/d_0 decrease. Hence, the obstacle reduces the speed and height of the downstream current by reducing its flux.

The simulations show that the maximum drag is approximately equal to the pressure force on the upstream face of the obstacle during the quasisteady state. Based on this observation, we use the present steady shallow water model to calculate this pressure force, thereby obtaining an estimate for the maximum drag. This estimate agrees well with the maximum drag calculated from the simulations for cases in which the obstacle height is much larger than the thickness of the boundary layer at the bottom wall.

Further work is required to analyze flows over obstacles involving larger, non-Boussinesq density differences (Lowe *et al.* (2005); Birman *et al.* (2005)), sloping bottom walls (Birman *et al.* (2007)) or obstacles that are small compared to the current height.

Acknowledgment

E. G.-J. is being supported by National Science Foundation IGERT grant DGE02-21715, as well as by a Cota-Robles fellowship. Computing time has been provided by the California NanoSystems Institute at UC Santa-Barbara and Hewlett-Packard.

REFERENCES

Armi, L. & Farmer, D. M. 1986 Maximal two-layer exchange through a contraction with barotropic net flow. *J. Fluid Mech.* **164**, 27–51.

Baines, P. 1995 *Topographic effects in stratified flows*. Cambridge University Press.

Benjamin, T. B. 1968 Gravity currents and related phenomena. *J. Fluid Mech.* **31**, 209–248.

Birman, V. K., Battandier, B. A., Meiburg, E. & Linden, P. F. 2007 Lock-exchange flows in sloping channels. *J. Fluid Mech.* **577**, 53–77.

Birman, V. K., Martin, J. E. & Meiburg, E. 2005 The non-Boussinesq lock-exchange problem. Part 2. High-resolution simulations. *J. Fluid Mech.* **537**, 125–144.

Braucher, E. P. 1950 Initial characteristics of density current flow. Master's thesis, MIT.

Britter, R. & Linden, P. 1980 The motion of the front of a gravity current travelling down an incline. *J. Fluid Mech.* **99**, 531–543.

Cantero, M., Lee, J., Balachandar, S. & Garcia, M. 2007 On the front velocity of gravity currents. *J. Fluid Mech.* **586**, 1–39.

Didden, N. & Maxworthy, T. 1982 The viscous spreading of plane and axisymmetric gravity currents. *J. Fluid Mech.* **121**, 27–42.

Ermanyuk, E. V. & Gavrilov, N. V. 2005*a* Interaction of an internal gravity current with a submerged circular cylinder. *J. Appl. Mech. Tech. Phys.* **46** (2), 216–223.

Ermanyuk, E. V. & Gavrilov, N. V. 2005*b* Interaction of an internal gravity current with an obstacle on the channel bottom. *J. Appl. Mech. Tech. Phys.* **46** (4), 489–495.

Ermanyuk, E. V. & Gavrilov, N. V. 2007 A note on the propagation speed of a weakly dissipative gravity current. *J. Fluid Mech.* **574**, 393–403.

Farmer, D. M. & Armi, L. 1986 Maximal two-layer exchange over a sill and through the combination of a sill and contraction with barotropic flow. *J. Fluid Mech.* **164**, 53–76.

Gonzalez-Juez, E. D., Constantinescu, S. G. & Meiburg, E. 2007 A study of the interaction of a gravity current with a square cylinder using two-dimensional numerical simulations. In *Proceedings of the 26th International Conference on Offshore Mechanics and Arctic Engineering*.

Gonzalez-Juez, E. D., Meiburg, E. & Constantinescu, S. G. 2008*a* Gravity currents impinging on submerged cylinders: Flow fields and associated forces. Submitted to J. Fluid Mech.

Gonzalez-Juez, E. D., Meiburg, E. & Constantinescu, S. G. 2008*b* The interaction of a gravity current with a circular cylinder mounted above a wall: Effect of the gap size. Submitted to J. Fluid Struct.

Greenspan, H. P. & Young, R. E. 1978 Flow over a containment dyke. *J. Fluid Mech.* **87** (Jul), 179.

Härtel, C., Meiburg, E. & Necker, F. 2000 Analysis and direct numerical simulation of the flow at a gravity-current head. Part 1. Flow topology and front speed for slip and no-slip boundaries. *J. Fluid Mech.* **418**, 189–212.

Hogg, A., Hallworth, M. & Huppert, H. 2005 On gravity currents driven by constant fluxes of saline and particle-laden fluid in the presence of a uniform flow. *J. Fluid Mech.* **539**, 349–385.

Hopfinger, E. J. 1983 Snow avalanche motion and related phenomena. *Ann. Rev. Fluid Mech.* **15**, 47–76.

Huppert, H. & Simpson, J. 1980 The slumping of gravity currents. *J. Fluid Mech.* **99**, 785–799.

Keulegan, G. H. 1958 The motion of saline fronts in still water. Nat. Bur. Stand. Rept. 5831.

Kneller, B., Bennett, S. J. & McCaffrey, W. D. 1999 Velocity structure, turbulence and fluid stresses in experimental gravity currents. *J. Geophys. Res. - Oceans* **104** (C3), 5381–5391.

Lane-Serff, G. F., Beal, L. M. & Hadfield, T. D. 1995 Gravity current flow over obstacles. *J. Fluid Mech.* **292**, 39–53.

Lowe, R. J., Rottman, J. W. & Linden, P. F. 2005 The non-Boussinesq lock-exchange problem. Part 1. Theory and experiments. *J. Fluid Mech.* **537**, 101–124.

Oehy, C. D. & Schleiss, A. J. 2007 Control of turbidity currents in reservoirs by solid and permeable obstacles. *J. Hydr. Engrg.* **133**, 637–648.

Ooi, S., Constantinescu, S. & Weber, L. 2005 Two-dimensional large eddy simulation of lock-exchange gravity current flows. In *Proceedings of the 31st International Association Hydraulic Research Congress*.

Pierce, C. D. 2001 Progress-variable approach for large eddy simulation of turbulent combustion. PhD thesis, Stanford University.

Pierce, C. D. & Moin, P. 2004 Progress-variable approach for large-eddy simulation of non-premixed turbulent combustion. *J. Fluid Mech.* **504**, 73–97.

Rottman, J. W. & Simpson, J. E. 1983 Gravity currents produced by instantaneous releases of a heavy fluid in a rectangular channel. *J. Fluid Mech.* **135** (Oct), 95–110.

Rottman, J. W., Simpson, J. E., Hunt, J. C. R. & Britter, R. E. 1985 Unsteady gravity current flows over obstacles: Some observations and analysis related to the phase II trials. *J. Hazard. Mater.* **11** (1-4), 325–340.

Shin, J. O., Dalziel, S. B. & Linden, P. F. 2004 Gravity currents produced by lock exchange. *J. Fluid Mech.* **521**, 1–34.

Simpson, J. E. 1997 *Gravity Currents in the Environment and the Laboratory*. Cambridge University Press.

Turner, J. S. 1973 *Buoyancy Effects in Fluids*. Cambridge University Press.

Wood, I. R. 1966 Studies in unsteady self preserving turbulent flows. Univ. of New South Wales, Water Research Lab., Rept. no. 81.

Woods, A. W., Bursik, M. I. & Kurbatov, A. V. 1998 The interaction of ash flows with ridges. *Bulletin of Volcanology* **60** (1), 38–51.